Title

Effects of kV, filtration, dose, and object size on soft tissue and iodine contrast in dedicated breast CT

Journal

Medical Physics, 47(7)

ISSN

0094-2405

Authors

Hernandez, Andrew M
Abbey, Craig K
Ghazi, Peymon
et al.

Publication Date

2020-07-01

DOI

10.1002/mp.14159

Peer reviewed

HHS Public Access

Author manuscript

Med Phys. Author manuscript; available in PMC 2021 July 01.

Published in final edited form as:

Med Phys. 2020 July ; 47(7): 2869–2880. doi:10.1002/mp.14159.

Effects of kV, filtration, dose, and object size on soft tissue and iodine contrast in dedicated breast CT

Andrew M. Hernandez[a)],
Department of Radiology, University of California Davis, Sacramento, CA 95817, USA

Craig K. Abbey,
Department of Psychological & Brain Sciences, University of California Santa Barbara, Santa Barbara, CA 93106, USA

Peymon Ghazi,
Malcova LLC, Baltimore, MD 21211, USA

George Burkett,
Department of Radiology, University of California Davis, Sacramento, CA 95817, USA

John M. Boone
Department of Radiology, University of California Davis, Sacramento, CA 95817, USA

Department of Biomedical Engineering, University of California Davis, Sacramento, CA 95817, USA

Abstract

Purpose: Clinical use of dedicated breast computed tomography (bCT) requires relatively short scan times necessitating systems with high frame rates. This in turn impacts the x-ray tube operating range. We characterize the effects of tube voltage, beam filtration, dose, and object size on contrast and noise properties related to soft tissue and iodine contrast agents as a way to optimize imaging protocols for soft tissue and iodine contrast at high frame rates.

Methods: This study design uses the signal-difference-to-noise ratio (SDNR), noise-equivalent quanta (NEQ), and detectability (d') as measures of imaging performance for a prototype breast CT scanner that utilizes a pulsed x-ray tube (with a 4 ms pulse width) at 43.5 fps acquisition rate. We assess a range of kV, filtration, breast phantom size, and mean glandular dose (MGD). Performance measures are estimated from images of adipose-equivalent breast phantoms machined to have a representative size and shape of small, medium, and large breasts. Water (glandular tissue equivalent) and iodine contrast (5 mg/ml) were used to fill two cylindrical wells in the phantoms.

Results: Air kerma levels required for obtaining an MGD of 6 mGy ranged from 7.1 to 9.1 mGy and are reported across all kV, filtration, and breast phantom sizes. However, at 50 kV, the thick

[a)]Author to whom correspondence should be addressed. amhern@ucdavis.edu.

CONFLICTS OF INTEREST

Authors AMH, PG, BK and JMB have patents (pending and issued) pertaining to breast CT. Author JMB has prior breast CT research support, licensing agreements with, and is a shareholder of Izotropic Imaging Corp. of Canada.

filters (0.3 mm of Cu or Gd) exceeded the maximum available mA of the x-ray generator, and hence, these conditions were excluded from subsequent analysis. There was a strong positive association between measurements of SDNR and d' ($R^2 > 0.97$) within the range of parameters investigated in this work. A significant decrease in soft tissue SDNR was observed for increasing phantom size and increasing kV with a maximum SDNR at 50 kV with 0.2 mm Cu or 0.2 mm Gd filtration. For iodine contrast SDNR, a significant decrease was observed with increasing phantom size, but a decrease in SDNR for increasing kV was only observed for 70 kV (50 and 60 kV were not significantly different). Thicker Gd filtration (0.3 mm Gd) resulted in a significant increase in iodine SDNR and decrease in soft tissue SDNR but requires significantly more tube current to deliver the same MGD.

Conclusions: The choice of 60 kV with 0.2 mm Gd filtration provides a good trade-off for maximizing both soft tissue and iodine contrast. This scanning technique takes advantage of the ~50 keV Gd k-edge to produce contrast and can be achieved within operating range of the x-ray generator used in this work. Imaging at 60 kV allows for a greater range in dose delivered to the large breast sizes when uniform image quality is desired across all breast sizes. While imaging performance metrics (i.e., detectability index and SDNR) were shown to be strongly correlated, the methodologies presented in this work for the estimation of NEQ (and subsequently d') provides a meaningful description of the spatial resolution and noise characteristics of this prototype bCT system across a range of beam quality, dose, and object sizes.

Keywords

breast CT; iodine contrast; MTF; NPS; spectral optimization; x-ray imaging

1. INTRODUCTION

Dedicated breast computed tomography (bCT) is a three-dimensional imaging modality based on x-ray computed tomography that is capable of rendering the internal structure of the breast at submillimeter resolution.[1–4] Advancements in imaging hardware,[3,5] image processing,[6,7] protocol optimization,[8–10] and dosimetry estimation[11–13] have improved the diagnostic capabilities of bCT, suggesting the possibility of superior detection of mass lesions compared to mammography.[14] As these systems move into clinical use, practical issues such as data acquisition rates and x-ray generator operating ranges become important considerations for finding optimal scanning protocols.

Several investigators have examined the selection of optimal kV and filtration combinations for dedicated breast CT at various conceptual levels including simulations,[10,15–19] benchtop systems,[8,10,18,20–23] and prototype scanners.[9] These studies came to conclusions for optimal kV and filtration ranging from 40 to 80 kV, and a variety of filter materials and thicknesses. This is to be expected given that the studies had different endpoints (soft tissue, calcifications, and iodine-based contrast), different scanner designs, and were conducted over a period of time in which imaging systems have changed considerably with hardware advancements. Studies investigating imaging performance for soft tissue contrast tended to favor lower kV and the performance decreased with increasing kV, while those evaluating iodine contrast found optimal performance at 50–60 kV, well above the 33.3 keV k-edge of Iodine.

Dedicated breast CT systems are being considered for a variety of clinical uses in breast cancer detection, diagnosis, and treatment monitoring. There is currently one commercial bCT product available (Koning Inc., West Henrietta, NY), which has been cleared by the FDA for diagnostic use as an adjunct to mammography in the USA. Other prototype scanners are being developed and evaluated in clinical trials.[5,24] Clinical use places important constraints on the x-ray generator as well as other components of the scanner. One such constraint is the need to perform a scan in a short period of time to minimize patient motion artifacts. Shorter scans necessitate higher data acquisition rates, which in turn necessitate higher x-ray tube current. Additionally, pulsed x-ray generators have the potential to substantially reduce motion blur from continuous acquisition,[5] but these put even more emphasis on high tube currents. This trade-off between optimal imaging and constraints of the x-ray tube is the motivation for this study.

The primary goal of this work is to carefully consider image quality under the constraints of tube power and an appropriate patient dose for high frame rate pulsed x-ray protocols. We focus on optimizing image quality for soft tissue contrast, and for contrast-enhanced imaging with an iodine contrast agent. These are two areas where bCT has already shown great promise.[1,14] In the diagnostic setting, accurate depiction of soft tissue and iodine will be crucial for discriminating between malignant and benign lesions. This work compares the use of Gd and Cu filtration for a range of tube potentials (50–70 kV) for both iodine contrast and soft tissue imaging tasks in breast CT using anatomically realistic shaped breast phantoms of various sizes. Gadolinium filtration was investigated in this work following recent studies by Glick et al. in which they found, using simulations[16] and later confirmed on a benchtop system,[8] that this choice of filtration can significantly reduce radiation dose without compromising image quality. The choice of 50 and 60 kV tube potentials is consistent with the optimal beam energy range determined by others.[8–10,17,22] A tube potential of 70 kV was used due to its relatively high output (compared with 50 and 60 kV with the same filtration), which reduces the impact of a limited x-ray tube operating range.

Imaging performance is quantified in reconstructed bCT images by means of the signal-difference-to-noise ratio (SDNR) at specified dose levels and various phantom sizes. We also calculate the modulation transfer function (MTF) and noise power spectrum (NPS), which are combined into the noise equivalent quanta (NEQ). Noise equivalent quanta are then used to compute a detectability index for comparison with SDNR. This allows us to assess the extent to which SDNR is associated with detection performance in a specific task. A subset of the optimal kV/filter combinations were then used to quantify the dose required to produce images of equivalent quality to that of an “average”-sized breast.

2. MATERIALS AND METHODS

2.A. Breast phantoms and contrast materials

Previously reported physical breast phantoms[12] were utilized in this work for all imaging tasks, dosimetry assessments, and image processing methods. The breast phantoms are classified by total breast volume and fabricated from ultra-high molecular weight polyethylene (UHMW). This material has a density of 0.941 g/cm^3 which is within 2% of the density of adipose tissue (0.93 g/cm^3). UHMW has been shown to be a satisfactory

surrogate material for the adipose component of breast parenchyma[9] over the energy ranges considered in this work. Three different breast phantoms corresponding to small (226 cm^3), average (614 cm^3), and large (1193 cm^3) breast sizes were used in this study and termed the V1, V3, and V5 phantoms, respectively — where the "V" denotes that volume was used for the classification. Two 15.6 mm diameter wells were machined at a radius of ~20 mm from the center of each phantom to a depth of ~60 mm (depending on phantom size) within the scanner field of view (FOV) when the phantoms were placed at the scanner isocenter. Solutions of distilled water and 5 mg/ml of iodine solution were used to fill each of the two wells in the phantom representing surrogate materials for glandular tissue and a contrast-enhanced lesion, respectively. Serial dilution was used to prepare the iodine solution using Visipaque™ and distilled water.

The phantoms used in this study are composed of materials with uniform attenuation coefficients that closely match adipose, fibroglandular, and contrast-enhanced tissues in breast imaging.[9,25,26] Noncontrast breast CT imaging of suspicious mass lesions usually involves localizing and characterizing relatively uniform glandular lesions against a uniform adipose background, or characterizing lesions as they emerge from a larger glandular region.[1,2] For contrast-enhanced imaging, regions of enhancement typically appear against a relatively uniform glandular-equivalent back-ground.[14] Therefore, we believe that the phantom design in this work using glandular-equivalent and dilute iodine-filled wells in the uniform, adipose-equivalent background is a reasonable approximation of the relevant attenuators in breast CT imaging.

2.B. X-ray technique selection

The Doheny breast CT scanner can operate at a maximum tube potential of 70 kV. Tube potentials of 50, 60, and 70 kV were investigated in this work with Gd filtration based on the findings of Glick et al.[8,16] In addition, Cu filtration was used for comparison with filtration that has been used in clinical breast CT imaging in our laboratory.[1,2,14,15] The filtration thickness of each material was chosen to minimize the difference in half value layer (HVL) as a function of tube potential across the range of filtration materials — considering available material thicknesses.

Gadolinium foils 0.1 mm thick were available for use in this study and they helped guide the selection of corresponding thickness of Cu. HVL measurements were made using a 0.6 cm^3 thimble ionization chamber (10 × 6–0.6 CT) connected to a model 9060 electrometer and a model 9010 readout unit (Radcal Corp., Monrovia, CA, USA). The chamber was positioned at the scanner isocenter and the center of the active volume was aligned with the central ray of the x-ray beam. HVL measurements in Al were made for 0.3 mm Gd (for consistency with Glick et al.) at 50, 60, and 70 kV. Various Cu filtration thicknesses were used to best match the measured HVL values for the Gd filter across all three kV settings. This assessment resulted in 0.3 mm Cu and 0.3 mm Gd filtration. Two additional filter thicknesses were chosen (0.2 mm Cu and 0.2 mm Gd) to investigate the effect of filter thickness and x-ray tube output requirements. A total of 12 different kV/filter combination were selected for the V1 (small), V3 (average), and V5 (large) phantoms.

2.C. Breast dosimetry considerations

The mean glandular dose (MGD) levels for the V1, V3, and V5 phantoms were set to the MQSA limit of 6 mGy for two view screening mammography for an *average* breast. This limit was chosen for two reasons. Both soft tissue contrast and iodinated contrast are relevant to screening, particularly for women at high risk that are currently served by gadolinium-enhanced MRI. Additionally, at 6 mGy, there is relatively little contribution from quantum noise (see Fig. 10). As a result, the relative findings at 6 mGy will scale to higher dose levels that could be used in a diagnostic setting. The x-ray techniques required to deliver 6 mGy to each phantom size were estimated using:

a. X-ray spectra generated by the tungsten anode spectral model specific to breast CT ($TASMICS_{bCT}$[27]),

b. Previously reported monoenergetic normalized glandular dose values for breast CT using the homogenous breast model[12] "$DgN(E)_{CT}$" for the V1, V3, and V5 phantoms

c. Air kerma measurements free-in-air as a function of mAs for the Doheny scanner.

All 12 x-ray spectra with different kV/filter combinations were modeled using $TASMICS_{bCT}$ by mathematically adding filtration until the modeled HVL values were equivalent to the measured HVL values described above. The modeled x-ray spectra were then used to spectrally weight the $DgN(E)_{CT}$ values resulting in 12 different polyenergetic DgN (pDgN) coefficients for each phantom size. Lastly, the air kerma (mGy per mAs) was measured for all kV/filter combinations by varying the tube current and fitting the air kerma as a function of mAs using linear regression. Multiplication of the breast size-dependent pDgN coefficients and air kerma measurements for a given kV/filter combination allow for the estimation of a specific mAs that delivers the target MGD level for a given phantom size.

2.D. Image acquisition

A detailed description of the prototype breast CT scanner "Doheny" at our institution has been previously reported, and therefore, only technical specifications relevant to the image acquisitions are reported in this work. Doheny is equipped with a 11.3 kW pulsed x-ray tube (M-1581, Varian Medical Systems, Salt Lake City, UT) that can operate up to 70 kV, and a CMOS flat-panel detector (Dexela 2923M, Varian Imaging Products, Palo Alto CA). For phantom imaging, the CMOS detector was operated in 2 × 2 binning high gain mode resulting in a 150 μm detector element "dexel" pitch. An x-ray tube pulse width of 4 ms and a pulse period of 23 ms (i.e., 43.5 frames per second) were used in order to reduce the total scan time as much as possible within the frame rate capabilities of the detector panel while providing consistent and reproducible tube output for each frame (i.e., air kerma per pulse) in the tomographic acquisition. A total of 500 projections were acquired for a complete 360° rotation, in 11.5 s.

A mechanical support frame was built using optical rails for each phantom in order to suspend and align the phantom in the scanner FOV, and the center of the phantom was positioned at the scanner isocenter using the positioning laser on the Doheny gantry. The

FOV boundary notch that was machined into the phantoms during fabrication[12] was used for careful alignment in the coronal plane — ensuring that the posterior boundary of the phantom was aligned with the boundary of the reconstructed volume. All 12 kV/filter combinations and all three phantom sizes were imaged. The 500 projection images acquired for each acquisition were reconstructed using a variation of the Feldkamp algorithm[28] enabling it to be run on a graphic processing unit (GPU). A Shepp-Logan apodization filter with a cutoff frequency, $f_C = 2 \times f_{nyquist}$, was implemented in the reconstruction of a 1024 × 1024 matrix with an isotropic voxel dimension of 150 μm resulting in 468, 674, and 895 coronal slices in order to reconstruct the entirety of the V1, V3, and V5 phantoms, respectively. Low frequency shading artifacts caused by beam hardening, photon scatter, and incomplete sampling of the Radon space in the circular cone beam geometry[29] were all corrected for using a recently reported shading artifact correction algorithm.[7] This algorithm uses an iterative application of image segmentation using a convolutional neural network (CNN) and low order polynomial parameterization of the adipose distribution to correct for the low frequency shading artifacts. In the present study using reconstructed images of homogenous phantoms, the segmentation was applied manually by masking the contrast rods and using a single threshold for segmentation of the UHMW from air.

2.E. Imaging performance assessment

The following sections describe both spatially dependent (SDNR) and frequency-dependent NEQ image quality metrics used to optimize the acquisition parameters (kV, filtration, dose) of the Doheny scanner for soft tissue and iodine contrast detection tasks.

The SDNR is an intuitive metric that is simple to measure and provides a quantitative assessment of both contrast and noise magnitude. However, it does not account for spatial frequency-dependent variations in image noise and out of plane noise correlation, nor does it include the spatial resolution characteristics of the imaging system which are important for detection tasks in breast CT. Given that the background regions of the phantoms used in this investigation are homogenous, anatomical noise is not included, and therefore, it is assumed that only the noise magnitude will be affected by changes in kV, filtration, phantom size, and glandular dose. In addition, the local spatial resolution is assumed to be approximately equal in the FBP reconstructions across all kV, filtration, dose, and breast phantom sizes investigated in this work. To account for spatial resolution and noise correlations, we assess frequency-dependent NEQ and task-specific detectability.

2.E.1. Signal-difference-to-noise ratio (SDNR)—Imaging performance under conditions of varying kV/filter combinations, phantom size, and imaging tasks was assessed by the SDNR which was measured in coronal images of the reconstructed bCT volume datasets for soft tissue contrast using the water-filled well (glandular surrogate; $\mu_{glandular}$) against the UHMW background (adipose surrogate; $\mu_{adipose}$) and for iodine contrast enhancement using the well filled with 5 mg/ml iodine solution (μ_{iodine}) against the water-filled well ($\mu_{glandular}$) background as shown in Fig. 1 and defined as follows.

$$SDNR_{iodine} = \frac{\bar{\mu}_{iodine} - \bar{\mu}_{glandular}}{\sigma_{glandular}} \quad (1)$$

$$SDNR_{softtissue} = \frac{\bar{\mu}_{glandular} - \bar{\mu}_{adipose}}{\sigma_{adipose}} \quad (2)$$

where $\bar{\mu}$ represents the average attenuation coefficient in the voxels of a circular regions of interest (ROI) (Fig. 1) and σ represents the standard deviation of the background regions (i.e., $\sigma_{glandular}$ for $SDNR_{\text{iodine}}$ and $\sigma_{adipose}$ for $SDNR_{\text{soft tissue}}$). The SDNR was calculated on a slice-by-slice basis and averaged across seven consecutive slices that were centered about the central ray in the bCT geometry. In addition, the SDNR was calculated as a function of z, starting at 2 mm from the posterior edge of the scanner FOV to 2 mm from the anterior boundary (bottom) of the wells. The 2 mm offset from the top and bottom of the well was used to avoid effects of incomplete sampling artifacts.

To assess the significance of observed effects in SDNR, we use a three-way ANOVA model for iodine and soft tissue SDNR separately. We evaluate main effects of kV, filtration, and phantom size, as well as interactions of these factors. Each SDNR has been replicated seven times in the seven consecutive coronal slices. The resulting *P*-values are adjusted for multiple comparisons using the Benjamini-Hochberg method[30] with a false discovery rate of 5% for the combined soft tissue and iodine contrast results.

2.E.2. Noise equivalent quanta and detectability index—The noise equivalent quanta (NEQ) is a frequency-dependent image performance metric that represents the number of quanta contributing to the image as formed by a perfect detector.[31,32] Formulation of the three-dimensional NEQ is as follows:

$$NEQ(f_x, f_y, f_z) = \pi f \frac{MTF^2(f_x, f_y, f_z)}{NPS(f_x, f_y, f_z)} \quad (3)$$

where MTF is the modulation transfer function, and NPS is the power spectrum of quantum noise. The πf factor accounts for radial sampling density and bounds the NEQ at low frequencies.[32–34]

The MTF was calculated using the circular edge method[35] adopted from the more general edge method[36,37] for both the glandular and iodine contrast inserts. A total of 50 coronal images centered about the central ray in the Doheny geometry were used for the MTF assessment. A square ROI surrounding the circular object (iodine or glandular; as shown in Fig. 1) was used from the CT volume datasets and the circular Hough transform was implemented to estimate the center of the circular object. The oversampled edge spread function (ESF) was computed by mapping the center of all voxels from their native cartesian coordinates to polar coordinates. All voxels were then binned based on their radial distance from the circular object centroid and smoothed using a Savitzky-Golay smoothing filter to reduce the impact of image noise and preserve the shape of the ESF. The oversampled ESF was then differentiated to compute the corresponding line-spread function (LSF). Lastly, a fast Fourier transform (FFT) was applied to the filtered LSF and the modulus of the FFT was calculated, resulting in the two-dimensional (2D) MTF in the coronal plane. The accuracy of the MTF estimation is highly dependent on the accuracy of the estimated center of the circle

on the CT images. An approach was used to iteratively sample around the initial center location and determine the location that maximizes the MTF using the integral of the MTF from 0 to f_{nyquist} as the figure-of-merit. Specifically, a rectangular grid of 37.5 μm intervals (1/4 of the reconstructed voxel size) was defined to be centered about the estimated centroid location and the MTF estimation was repeated until a maximum MTF value was obtained. The MTF was calculated separately for all 50 coronal images and averaged to produce a single, low noise MTF.

The three-dimensional NPS was estimated in order to quantify the noise texture. Image subtraction was used for detrending and multiple volume of interest (VOI) ensembles were used for the NPS estimation, computed as follows:

$$NPS(f_x, f_y, f_z) = \frac{\Delta_x \Delta_y \Delta_z}{N_x N_y N_z} \frac{\sum_{i=1}^{N_{VOI}} |FFT_{3D}[DI_i(x, y, z)]|^2}{2 \times N_{VOI}} \quad (4)$$

where DI_i is the difference image (in units of attenuation coefficient) for the i-th VOI, Δ_x,Δ_y, and Δ_z are the three dimensions of each voxel, and N_x, N_y, and N_z are number of pixels in the VOIs in each dimension. The 2 in the denominator accounts for doubling of the noise variance in the image subtraction step. A total of 32 VOIs ($N_{VOI} = 32$) were used in the NPS assessment, centered about a constant radius equal to half the phantom radius, and equally spaced in 360°. As a proof of principle, the variance measured in the ROIs used for the NPS estimation in the CT reconstructions (before detrending) was compared against the integral of the NPS. While the fully three-dimensional (3D) NPS is a complete description of the image noise in a CT volume dataset, a human observer typically interprets images based on a 2D slice. To obtain a meaningful estimation of the 2D NPS, the 3D NPS must be integrated over the orthogonal direction (z) in order to account for noise correlation in adjacent slices.[38] The two-dimensional noise equivalent quanta (NEQ) were then computed using the 2D MTF and 2D NPS estimations (accounting for noise correlation in z) for each kV/filter combination.

The 2D slice detectability index (d'_{slice}) was estimated according to a task-based methodology summarized in ICRU 54[31] which quantifies imaging performance with respect to how well an observer performs a specific task given a 2D slice of a three-dimensional (3D) CT volume datasets.

$$d'^2_{slice} = \iint \frac{MTF_{2D}^2}{NPS_{2D}} W_{Task}^2(f_x, f_y) df_x df_y \quad (5)$$

where W_{task} is the task function which is a frequency representation of the imaging task (i.e., the disk in a 2D image) multiplied by the difference in the attenuation coefficients between the signal (iodine or glandular) and the corresponding backgrounds (glandular or adipose, respectively) at the specific energy and filtration of the beam. The detectability index provides a single, objective figure of merit with a SNR-like interpretation that can be used for system design and protocol optimization by combining traditional imaging performance metrics such as the MTF and NPS, with a task function specific to the imaging

task at hand. Estimations of d' were subsequently compared against the SDNR measurements (Section 2.E.1).

3. RESULTS

3.A. X-ray technique requirements

Table I outlines the air kerma levels required to deliver a target MGD of 6 mGy for the small (V1), medium (V3), and large (V5) breast phantom sizes. The measured HVL for each kV/filter combination is also shown in the table. Filtration thicknesses of 0.2 mm for Gd and 0.2 mm for Cu minimized the differences in HVL for the three tube potentials investigated with differences less than 5% across all kV settings. To investigate x-ray spectra with more filtration (i.e., higher penetrability), filtration thickness of 0.3 mm for Gd and 0.3 mm for Cu was also chosen because they minimized the differences in HVL across all kV settings investigated. Tube current requirements for each kV/filter combination are plotted in Fig. 2. For 50 kV, the mA required to deliver 6 mGy MGD for filtration choices of 0.3 mm Cu & 0.3 mm Gd is beyond the power limits of the tube on the Doheny scanner. Alternatively, the x-ray tube pulse width could be increased from 4 ms in order to increase the mAs per projection, but this would result in an increase in the scan time with subsequent motion blurring, both of which are undesirable effects. For example, generating enough tube output to deliver 6 mGy for a 50 kV/0.3 mm Gd spectrum would require approximate doubling of the pulse width to 8 ms and this would have a combined effect of increasing the scan time by 2 s and the motion blur by 70% at 7 cm from the isocenter. Figure 3 is a plot of the modeled x-ray spectra for 50 and 70 kV with 0.2 mm Cu and 0.2 mm Gd filtration with the photon fluence scaled to the air kerma required to deliver 6 mGy to the V3 phantom.

3.B. Imaging performance

Figure 4 depicts the SDNR results for iodine contrast (left column) and soft tissue (right column) plotted separately for each phantom size. Note that 50 kV with both 0.3 mm Cu and 0.3 mm Gd is not included since the mA required to deliver 6 mGy MGD for these kV/filter combinations is beyond the x-ray tube upper power limit on the Doheny scanner. The values reported in Fig. 4 can easily be used to obtain SDNR predictions at higher dose levels by normalizing the SDNR values by $\sqrt{MGD}$ using an MGD of 6 mGy and then multi-plying by the square root of the desired MGD.

The system MTF results are shown in Fig. 5, displayed as a radial average of the 2D MTF for the V3 phantom. The results show the average MTF profile for both imaging tasks and all 10 kV/filter combinations along with the minimum and maximum values at each spatial frequency. The average MTF at 50% was 1.31 lp/mm with a mean absolute difference of 1.9% across the 10 comparisons. In addition, the average MTF at 10% was 2.42 lp/mm with a mean absolute difference of 2.2%. Slight differences in the MTF across the 10 comparisons are likely the result of noise remaining in the ESFs. Despite these variations, the differences were all less than 4.2% supporting the notion that the MTF is independent of the kV/filter combinations used in this study.

An example of the 3D NPS for the V3 phantom scanned with 50 kV/0.2 mm Gd is shown in Figs. 6(a)–6(c). The coronal NPS demonstrates a band-pass frequency characteristic representative of filtered back projection. In comparison, the sagittal and axial NPS exhibit effects of a null cone around the f_z axis that is indicative of frequencies missing in the bCT volume data due to incomplete sampling from the cone beam geometry. Figure 6(d) shows a comparison plot of the radial average of the central slice through the 3D NPS for 0.2 mm Gd and 0.2 mm Cu filtration and both 50 and 70 kV. For ease in visual comparison the 0.3 mm Gd, 0.2 mm Cu, and all 60 kV results are not shown in Fig. 6(d). The variance, calculated as the integral of the 3D NPS, was within 0.1% of the variance computed within the VOIs in the spatial domain — verifying the Fourier transform operation used to compute the 3D NPS in Eq. (3). Figure 6(d) clearly demonstrates that only the magnitude of the noise varies between the different kV/filter combinations as expected. The mean noise standard deviation was 0.0270 mm^{-1} and 0.0237 mm^{1} for 0.2 mm Gd filtration at 50 and 70 kV, respectively. For 0.2 mm Cu, the noise was 0.0282 mm^{-1} and 0.0240 mm^{-1} at 50 and 70 kV, respectively — indicative of higher noise levels for lower tube potentials due to less photon penetration through the breast.

Two dimensional NEQ results are shown in Fig. 7 displayed as radially averaged profiles of the 2D NEQ after the bandwidth integral of the 3D NPS [example shown in Figs. 5(a)–5(c)] along the direction orthogonal to the slice (f_z direction). The present formulation of the NEQ [Eq. (3)] does not include the gain term. This ensures that factors related to the imaging system are included in the NEQ and factors related to the object (e.g., contrast) are included in the task [W_{task} in Eq. (5)].[31,32] MTF (Fig. 5) and NPS (Fig. 6) measurements were combined with the task function to provide a single figure of merit, d'.[2] The detectability index is plotted in Fig. 8 against the image domain-based SDNR measurements for the V3 phantom and all 10 kV/filter combinations. A strong linear correlation was observed between d' and SDNR indicating that within the range of techniques, imaging tasks, and phantoms investigated in this work the SDNR is a reasonable surrogate for the detectability index. With this observed correlation, the SDNR can be used to draw conclusions related to imaging of both iodine contrast and soft tissue across a range of kV/filter combinations which was the goal of the present work.

Results of the three-way ANOVA indicated highly significant ($P < 0.001$) main effects of kV, filtration, and phantom size, as well as interactions of these factors. Note that the 50 kV 0.3 mm Gd and 50 kV 0.3 mm Cu are considered as censored data in the analysis. As a result, the fitted ANOVA model explains 210 observations with 22 degrees of freedom. As seen in Fig. 4, SDNR decreases with increasing phantom size, which supports the understanding that for fixed dose image quality will vary depending on breast size. This decrease is more pronounced for soft tissue than for iodine contrast, meaning that beam-hardening affects soft tissue more than iodine contrast. In addition, the results indicate a general decrease in SDNR with increasing tube potential consistent with the findings of others.[8,14] However, the decrease in SDNR was monotonic with increasing kV only for soft tissue. For iodine SDNR, a significant decrease was only observed for 70 kV (no statistically significant difference was observed between 50 and 60 kV). This result is indicative of the k-edge of Gd at ~50 keV which shapes the 60 kV spectrum such that the majority of the fluence is within the energy range just above the k-edge of iodine. This has the effect of mitigating the reduction

in SDNR as tube potential increases from 50 to 60 kV. At 70 kV, the majority of the spectral fluence is concentrated well above the k-edge of iodine (even with Gd filtration) which decreases iodine contrast and results in a significant decrease in iodine SDNR relative to 50 and 60 kV.

In terms of comparing the effects of filtration material and thickness, the results indicate that while increasing the amount of Gd filtration increased the iodine SDNR, it resulted in a decrease in soft tissue SDNR and requires nearly 2× more tube current to deliver the same dose (see Fig. 2). Together these results indicate that increasing the filtration thickness is not advantageous in optimizing the imaging protocol for soft tissue and iodine contrast combined because it decreases the soft tissue SDNR and requires x-ray tube power beyond the upper limit of the bCTscanner under investigation.

The SDNR as a function of position from the posterior to anterior region of the contrast well [see Fig. 1(b)] in the V3 breast phantom is shown in Fig. 9. As expected, the SDNR tends to increase from the posterior to anterior region as a result of shorter path lengths through the breast, and the resulting reduction in noise and scatter. Within the 50 mm region shown in the figure, an increase in SDNR of ~50% was observed and the results are similar for all kV/filter combinations. Results shown in Fig. 10 demonstrate the variation in SDNR resulting from variations in MGD at a technique of 60 kV with 0.2 mm Gd. For both the iodine and soft tissue imaging tasks, an MGD of ~1.5 mGy for the V1 phantom would be sufficient for matching the SDNR of the V3 phantom (at 6 mGy) and a dose of ~12 mGy would be sufficient for the V5 phantom. Together these results indicate that a large variation in dose is required to deliver equivalent image quality, quantified by means of the SDNR, across all phantom sizes.

4. DISCUSSION

The present study measured the performance of Doheny, a prototype breast CT system at UC Davis, for soft tissue and iodine detection tasks in breast-shaped phantoms for tube potentials from 50 to 70 kV with both a beam softening filter (Gd with a k-edge of 50 keV) and conventional Cu filtration. Consistent with the findings of others,[8–10,16] 50–60 kV proved to be the ideal tube potential for both soft tissue and iodine contrast enhancement imaging, quantified by means of the SDNR and detectability index in the present study. For maximizing soft tissue SDNR, 50 kV is the optimal tube potential, and for iodine contrast SDNR no difference was observed between 50 and 60 kV. If the imaging protocol therefore does not include iodine contrast injection, then imaging at 50 kV would maximize the image quality. For iodine contrast protocols, imaging at 60 kV with Gd filtration takes advantage of the k-edge of Gd and requires 2–3 times less tube current than 50 kV with no observable difference in iodine SDNR.

These protocol designs are further complicated when equivalent image quality is preferred across all breast sizes, which was shown to require nearly twice the dose for the large breast compared against the average breast size. For the Doheny bCT scanner at UC Davis this would nearly double the tube and generator power requirements from 11 to 22 kW to preserve the short pulse width (4 milliseconds) scan protocol that reduces motion blur,

minimizes total scan time and preserves spatial resolution. In addition, 0.2 mm of Gd filtration is preferred over a thicker filter (0.3 mm Gd), because while 0.3 mm Gd results in an increase in iodine SDNR it decreases soft tissue SDNR (see Fig. 4), and thicker filters require two times more tube current than the corresponding thin filter as shown in Fig. 2. A tube/filter combination of 60 kV with 0.2 mm Gd therefore provides a good tradeoff between maximizing both soft tissue and iodine contrast by taking advantage of the ~50 keV Gd k-edge and minimizing tube power requirements of the existing bCT system investigated in this work. The M-1581 (Varian Medical Systems, Salt Lake City, UT) x-ray tube used in this study has a heat loading capacity of 1500 kHU. A bCT scan using the imaging protocol outlined in Section 2.D generates 27.4 kHU and 9.8 kHU for 0.2 mm Gd filtration with a tube potential of 50 and 70 kV, respectively — well within the heat capacity of the M-1581 x-ray tube.

Previous studies have compared new x-ray techniques against filtration materials and thicknesses that are consistent with commercial and some prototype bCT scanners in order to gain important insight into the potential for dose reduction using exotic filtration materials. However, the noise in a CT filtered-back projection reconstruction is inversely proportional to the square root of the number of incident quanta at the detector. Therefore, comparing image quality metrics using spectra with significantly different x-ray beam penetrability (i.e., HVL) masks the ability to compare the effects of the filtration materials directly. For this reason, filtration thicknesses for each material were chosen in this study such that they provide similar HVLs for the range of tube potentials investigated.

The decision to investigate Gd filtration was based upon the findings of Glick et al. for iodinated contrast-enhanced bCT in which they demonstrated that imaging with 49 kV and Gd or Er filtration provides up to ~250% improvement in dose efficiency compared to conventional filtration used on commercial and prototype bCT systems.[8] The simulated and measured results by Glick's group indicate that by simply shaping the x-ray spectrum specifically for iodine contrast detection, a significant improvement in detectability can be achieved. However, their results were for 49 kV with Gd/Er filtration against 80 kV with 0.3 mm Cu filtration and therefore only the combined effect of both tube potential and filtration was assessed. Furthermore, materials like Gd and Er are advantageous for iodine imaging because they have k-edges (50.2 and 57.5 keV, respectively) above the k-edge of iodine (33.2 keV) and therefore can shape the spectrum for improved iodine-to-glandular contrast. However, imaging at 49 kV does not take advantage of this beam shaping effect of Er or Gd filtration and requires significantly more x-ray tube output than imaging at high tube potentials, especially at high frame rates as demonstrated in the present work.

The Fourier-based metrics presented in this work for estimation of the signal (MTF) and noise (NPS) transfer characteristics requires the assumption of linearity, local shift invariance, and local stationarity for the imaging system under investigation. All volume data sets used in this work were reconstructed using FBP which satisfies the assumption of linearity and local shift invariance. In addition, it is well understood that location of the ensemble VOIs used for the NPS estimation affects the shape of spectrum and therefore the wide-sense stationary assumption is not satisfied entirely.[39,40] All VOIs were therefore chosen to be centered at a constant radius within the phantom (which was centered about the

scanner isocenter) and equally spaced in 360° to more closely approximate wide-sense stationary. Lastly, due to the incomplete sampling of the Radon space inherent in the cone beam geometry the point spread function is likely non-stationary. To address this, the MTF was measured in a region which was centered about the central ray and therefore incomplete sampling was minimized; however, these limitations must be considered when interpreting these results.

Accurate MTF estimation requires accurate geometrical calibration, high precision machining of the test object, and quantum noise mitigation. Given the high spatial resolution capabilities of some modern flat panel detectors, such as the Dexela panel installed on Doheny, these requirements are even more stringent. The “BB” geometrical calibration method[41] was used for calibration of Doheny and a fine tuning of the central ray location incident on the detector was iteratively determined to optimize the MTF. All wells in the breast phantoms were machined using a high-performance CNC mill and caution was taken to provide a smooth surface finish. Remaining surface inconsistencies are likely beyond the spatial resolution limitations of the Doheny scanner; however, they are a limitation of this study. Quantum noise was mitigated in the MTF noise estimations by averaging two scans, averaging multiple coronal images, and oversampling the edge spread function.

This work and previously reported studies on spectral optimization in bCT used glandular dose estimations for the simple homogenous breast model which has recently been shown to result in an overestimation of normalized glandular dose coefficients for breast CT.[11,13] With this in mind, the SDNR measurements in this work were then normalized by glandular dose estimations using a heterogenous breast dosimetry model[11] and compared against a simple homogenous model.[12] Taking into account previously published breast dosimetry estimations using a more anatomically accurate heterogenous breast dosimetry model, the change in MGD estimated using the heterogenous model (MGD_{hetero}) relative to the homogenous model was on average −1.4% [range = −5.7% to 1.8%] across the range of kV, filtration, and breast sizes investigated in this work. The difference in SDNR when normalized by $\sqrt{MGD_{hetero}}$ relative to normalization by $\sqrt{MGD_{homo}}$ was on average 2.4%, 1.2%, and 0.6% for 50, 60, and 70 kV, respectively, averaged across phantom sizes and the two thin filtration choices (0.2 mm Cu and 0.2 mm Gd). The differences were 0.2% and −0.3% for 60 and 70 kV, respectively, averaged across phantom sizes and the two thick filtration choices (0.3 mm Cu and 0.3 mm Gd). Together these results indicate that differences in the estimation of MGD using the more anatomically accurate heterogenous breast dosimetry models result in only a minimal difference in the dose weighted SDNR metric.

The breast phantoms utilized in this work were composed of a homogenous background and therefore did not take into account the anatomical variability inherent in a patient’s breast parenchyma. Several important questions remain including how adding background variability in the breast phantoms would affect imaging tasks such as size discrimination, low contrast detectability, as well as detection and localization of microcalcifications. The methods here establish optimal scanning techniques for a high frame rate, pulsed x-ray tube scanner for tasks with a uniform background, but these may need revision for other imaging tasks. In particular, specific phantoms related to microcalcifications will need to be

developed to optimize these systems because of challenges related to resolution and dose limitations.

5. CONCLUSIONS

A tube potential of 60 kV with 0.2 mm Gd provides a good tradeoff between maximizing both soft tissue and iodine contrast by taking advantage of the ~50 keV Gd k-edge and minimizing tube power requirements of the existing bCT system investigated in this work. Imaging at 60 kV allows for a greater range in dose delivered to the large breast sizes when uniform image quality is desired across all breast sizes. While imaging performance metrics (i.e., detectability index and SDNR) were shown to be strongly correlated, the methodologies presented in this work for the estimation of NEQ (and subsequently d') provides a meaningful description of the spatial resolution and noise characteristics of this prototype bCT system across a range of beam quality, dose and breast sizes. Future work should incorporate a similar NEQ type approach for systematic optimization of other imaging tasks.

ACKNOWLEDGMENTS

The authors thank Stephen Glick for stimulating discussions and for sharing some filtration materials for preliminary experiments. This research was supported by research grants (RO1 CA181081 & R01 EB025829) from the National Cancer Institute. The content is solely the responsibility of the authors and does not necessarily represent the official views of the National Cancer Institute or the National Institutes of Health.

REFERENCES

1. Lindfors KK, Boone JM, Nelson TR, Yang K, Kwan AL, Miller DF. Dedicated breast CT: initial clinical experience. Radiology. 2008;246: 725–733. [PubMed: 18195383]
2. O'Connell A, Conover DL, Zhang Y, et al. Cone-beam CT for breast imaging: radiation dose, breast coverage, and image quality. AJR Am J Roentgenol. 2010;195:496–509. [PubMed: 20651210]
3. Kalender WA, Beister M, Boone JM, Kolditz D, Vollmar SV, Weigel MC. High-resolution spiral CT of the breast at very low dose: concept and feasibility considerations. Eur Radiol. 2012;22:1–8. [PubMed: 21656331]
4. McKinley RL, Tornai MP, Tuttle LA, Steed D, Kuzmiak CM. Development and initial demonstration of a low-dose dedicated fully 3D breast CT system In: International Workshop on Digital Mammography. Vol. 7361, Berlin, Heidelberg: Springer; 2012:442–449.
5. Gazi PM, Yang K, Burkett GW Jr, Aminololama-Shakeri S, Seibert JA, Boone JM. Evolution of spatial resolution in breast CT at UC Davis. Med Phys. 2015;42:1973–1981. [PubMed: 25832088]
6. Caballo M, Boone JM, Mann R, Sechopoulos I. An unsupervised automatic segmentation algorithm for breast tissue classification of dedicated breast computed tomography images. Med Phys. 2018;45:2542–2559. [PubMed: 29676025]
7. Ghazi P, Hernandez AM, Abbey C, Yang K, Boone JM. Shading artifact correction in breast CT using an interleaved deep learning segmentation and maximum-likelihood polynomial fitting approach. Med Phys. 2019;46:3414–3430. [PubMed: 31102462]
8. Makeev A, Glick SJ. Low-dose contrast-enhanced breast CT using spectral shaping filters: an experimental study. IEEE Trans Med Imaging. 2017;36:2417–2423. [PubMed: 28783629]
9. Prionas ND, Huang SY, Boone JM. Experimentally determined spectral optimization for dedicated breast computed tomography. Med Phys. 2011;38:646–655. [PubMed: 21452702]
10. Weigel M, Vollmar SV, Kalender WA. Spectral optimization for dedicated breast CT. Med Phys. 2011;38:114–124. [PubMed: 21361181]

11. Hernandez AM, Becker AE, Boone JM. Updated breast CT dose coefficients (DgNCT) using patient-derived breast shapes and heterogeneous fibroglandular distributions. Med Phys. 2019;46:1455–1466. [PubMed: 30661250]
12. Hernandez AM, Boone JM. Average glandular dose coefficients for pendant-geometry breast CT using realistic breast phantoms. Med Phys. 2017;44:5096–5105. [PubMed: 28715130]
13. Sechopoulos I, Bliznakova K, Qin X, Fei B, Feng SS. Characterization of the homogeneous tissue mixture approximation in breast imaging dosimetry. Med Phys. 2012;39:5050–5059. [PubMed: 22894430]
14. Prionas ND, Lindfors KK, Ray S, et al. Contrast-enhanced dedicated breast CT: initial clinical experience. Radiology. 2010;256:714–723. [PubMed: 20720067]
15. Chen B, Ning R. Cone-beam volume CT breast imaging: feasibility study. Med Phys. 2002;29:755–770. [PubMed: 12033572]
16. Glick SJ, Makeev A. Investigation of x-ray spectra for iodinated contrast-enhanced dedicated breast CT. J Med Imaging (Bellingham). 2017;4:013504. [PubMed: 28149923]
17. McKinley RL, Tornai MP, Samei E, Bradshaw ML. Simulation study of a quasi-monochromatic beam for x-ray computed mammotomography. Med Phys. 2004;31:800–813. [PubMed: 15124997]
18. Boone JM, Nelson TR, Lindfors KK, Seibert JA. Dedicated breast CT: radiation dose and image quality evaluation. Radiology. 2001;221: 657–667. [PubMed: 11719660]
19. Glick SJ, Thacker S, Gong X, Liu B. Evaluating the impact of x-ray spectral shape on image quality in flat-panel CT breast imaging. Med Phys. 2007;34:5–24. [PubMed: 17278485]
20. Ning R, Conover D, Lu XH, et al. Evaluation of flat panel detector cone beam CT breast imaging with different sizes of breast phantoms. Proc Spie. 2005;5745:626–636.
21. Lai CJ, Shaw CC, Chen L, et al. Visibility of microcalcification in cone beam breast CT: effects of X-ray tube voltage and radiation dose. Med Phys. 2007;34:2995–3004. [PubMed: 17822008]
22. Crotty DJ, McKinley RL, Tornai MP. Experimental spectral measurements of heavy K-edge filtered beams for x-ray computed mammotomography. Phys Med Biol. 2007;52:603–616. [PubMed: 17228108]
23. Silkwood JD, Matthews KL, Shikhaliev PM. Photon counting spectral breast CT: effect of adaptive filtration on CT numbers, noise, and contrast to noise ratio. Med Phys. 2013;40:051905. [PubMed: 23635275]
24. Berger N, Marcon M, Saltybaeva N, et al. Dedicated breast computed tomography with a photon-counting detector: initial results of clinical in vivo imaging. Invest Radiol. 2019;54:409–418. [PubMed: 30829942]
25. Ivanov D, Bliznakova K, Buliev I, et al. Suitability of low density materials for 3D printing of physical breast phantoms. Phys Med Biol. 2018;63:175020. [PubMed: 29999497]
26. Johns PC, Yaffe MJ. X-ray characterisation of normal and neoplastic breast tissues. Phys Med Biol. 1987;32:675–695. [PubMed: 3039542]
27. Hernandez AM, Seibert JA, Nosratieh A, Boone JM. Generation and analysis of clinically relevant breast imaging x-ray spectra. Med Phys. 2017;44:2148–2160. [PubMed: 28303582]
28. Feldkamp LA, Davis LC, Kress JW. Practical cone-beam algorithm. J Opt Soc Am A. 1984;1:612–619.
29. Zhu L, Starman J, Fahrig R. An efficient estimation method for reducing the axial intensity drop in circular cone-beam CT. Int J Biomed Imaging. 2008;2008:242841. [PubMed: 18923681]
30. Benjamini Y, Hochberg Y. Controlling the false discovery rate: a practical and powerful approach to multiple testing. J Roy Stat Soc: Ser B (Methodol). 1995;57:289–300.
31. Vennart W ICRU. Report 54: Medical imaging - the assessment of image quality. Radiography. 1997;3:243–244. ISBN 0–913394-53-X.
32. Tward DJ, Siewerdsen JH. Noise aliasing and the 3D NEQ of flat-panel cone-beam CT: effect of 2D/3D apertures and sampling. Med Phys. 2009;36:3830–3843. [PubMed: 19746816]
33. Tward DJ, Siewerdsen JH. Cascaded systems analysis of the 3D noise transfer characteristics of flat-panel cone-beam CT. Med Phys. 2008;35: 5510–5529. [PubMed: 19175110]
34. Hanson KM. Detectability in computed tomographic images. Med Phys. 1979;6:441–451. [PubMed: 492079]

35. Takenaga T, Katsuragawa S, Goto M, Hatemura M, Uchiyama Y, Shiraishi J. Modulation transfer function measurement of CT images by use of a circular edge method with a logistic curve-fitting technique. Radiol Phys Technol. 2015;8:53–59. [PubMed: 25142743]

36. Judy PF. The line spread function and modulation transfer function of a computed tomographic scanner. Med Phys. 1976;3:233–236. [PubMed: 785200]

37. Samei E, Flynn MJ, Reimann DA. A method for measuring the presampled MTF of digital radiographic systems using an edge test device. Med Phys. 1998;25:102–113. [PubMed: 9472832]

38. Siewerdsen JH, Cunningham IA, Jaffray DA. A framework for noise-power spectrum analysis of multidimensional images. Med Phys. 2002;29:2655–2671. [PubMed: 12462733]

39. Pineda AR, Tward DJ, Gonzalez A, Siewerdsen JH. Beyond noise power in 3D computed tomography: the local NPS and off-diagonal elements of the Fourier domain covariance matrix. Med Phys. 2012;39: 3240–3252. [PubMed: 22755707]

40. Dolly S, Chen HC, Anastasio M, Mutic S, Li H. Practical considerations for noise power spectra estimation for clinical CT scanners. J Appl Clin Med Phys. 2016;17:392–407.

41. Yang K, Kwan AL, Miller DF, Boone JM. A geometric calibration method for cone beam CT systems. Med Phys. 2006;33:1695–1706. [PubMed: 16872077]

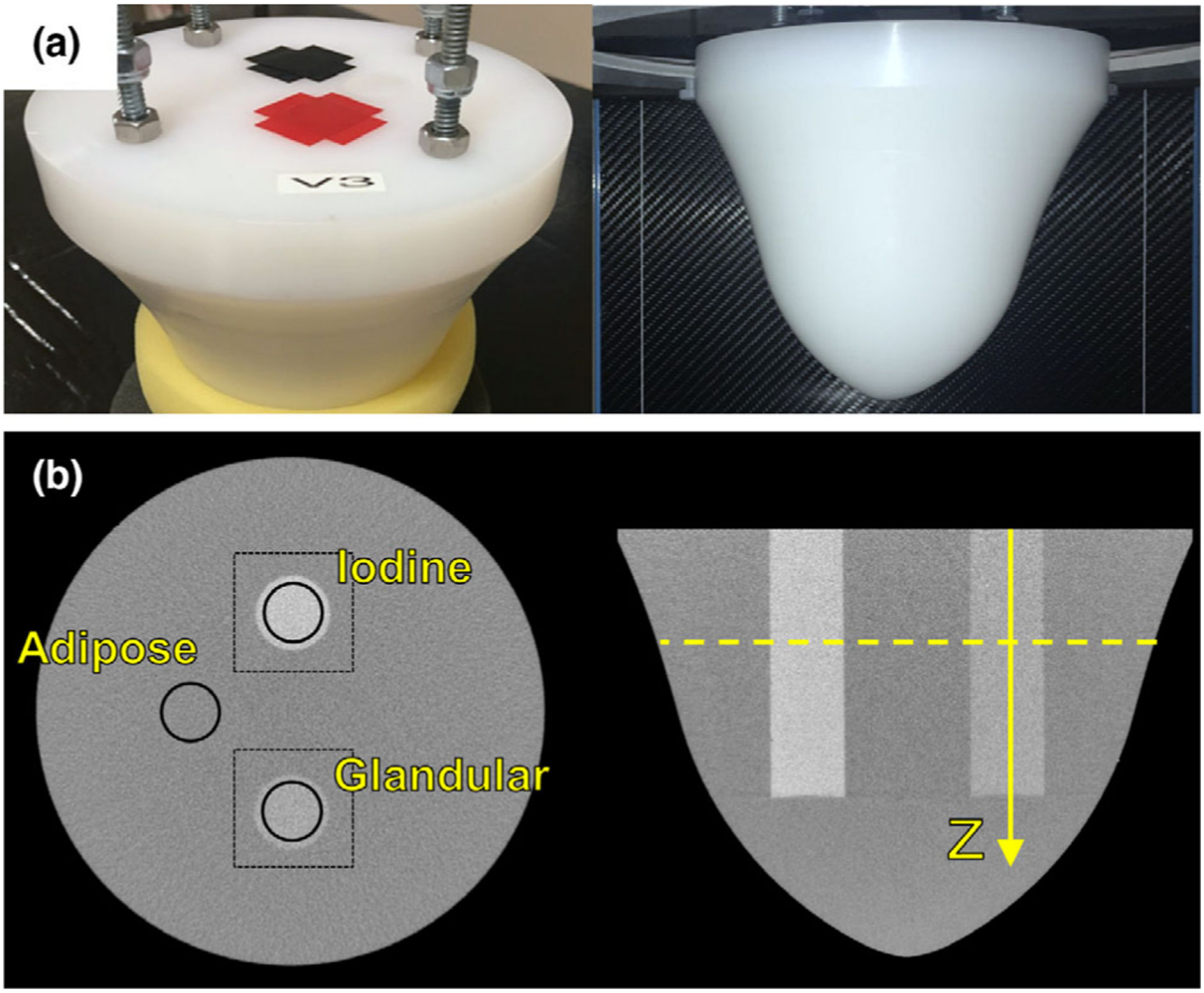

Fig. 1.

(a) Photographs of the V3 phantom contrast wells (red- and black-taped “x” marks) and the phantom suspended in the breast computed tomography scanner field of view. (b) Example coronal and sagittal slices through the V3 phantom reconstructions depicting the location of the iodine, glandular, and adipose regions. The circular ROIs in the coronal image depict the regions used for the signal-difference-to-noise ratio measurements and the contrast term in the task function for the detectability index. The dotted square ROIs indicate the region where the modulation transfer function calculation was performed.

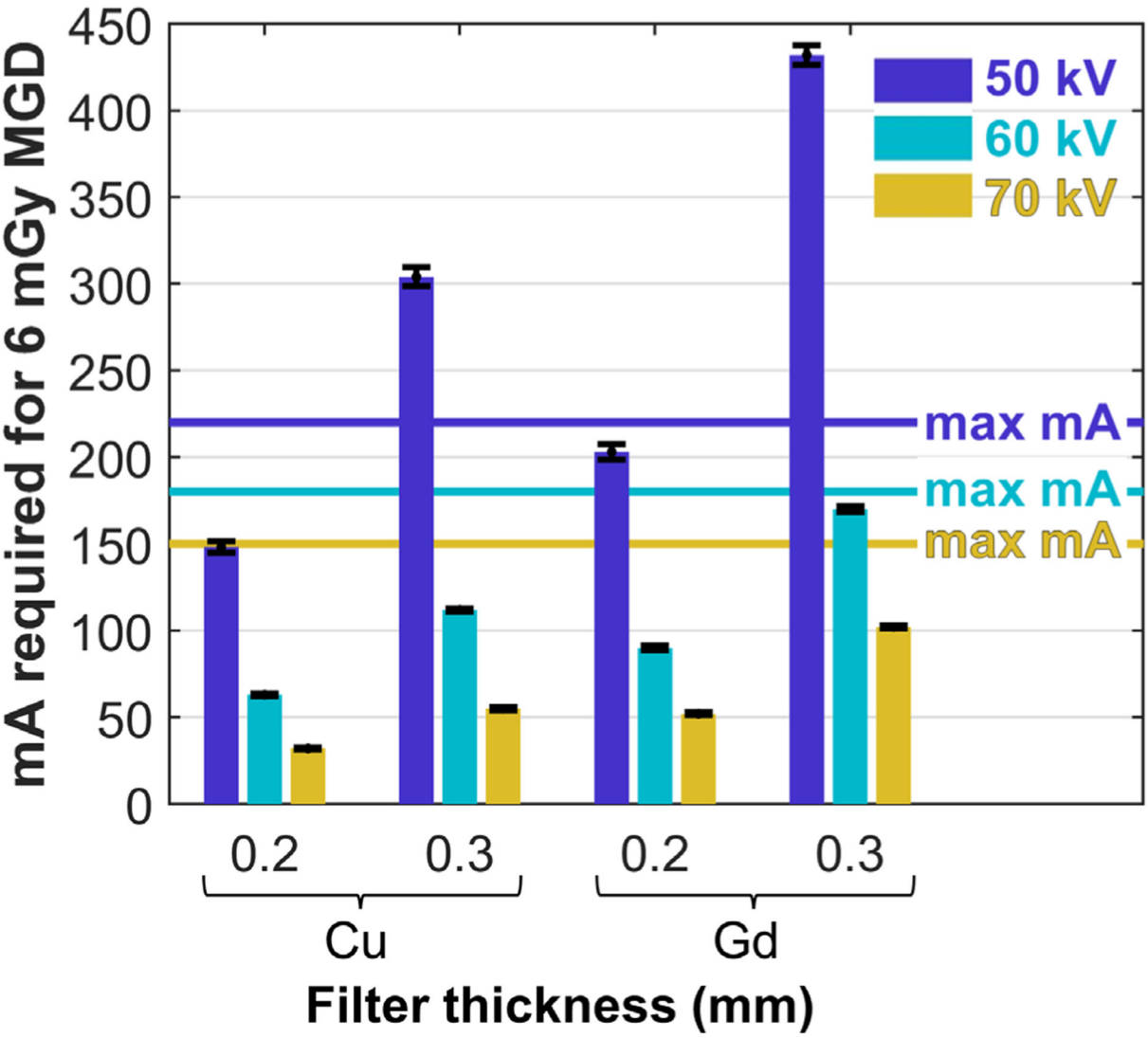

Fig. 2.

Tube current (mA) required for each kV/filter combination in order to deliver the target mean glandular dose of 6 mGy. Results shown are the average +/− one standard deviation across all three phantom sizes. The solid horizontal lines indicate the max mA allowed for the Doheny scanner which corresponds to 220, 180, and 150 mA at 50, 60, and 70 kV, respectively. Specifically, for the thicker filtration choices at 50 kV (0.3 mm Cu & 0.3 mm Gd), the required mA is beyond the power limitations of the scanner investigated.

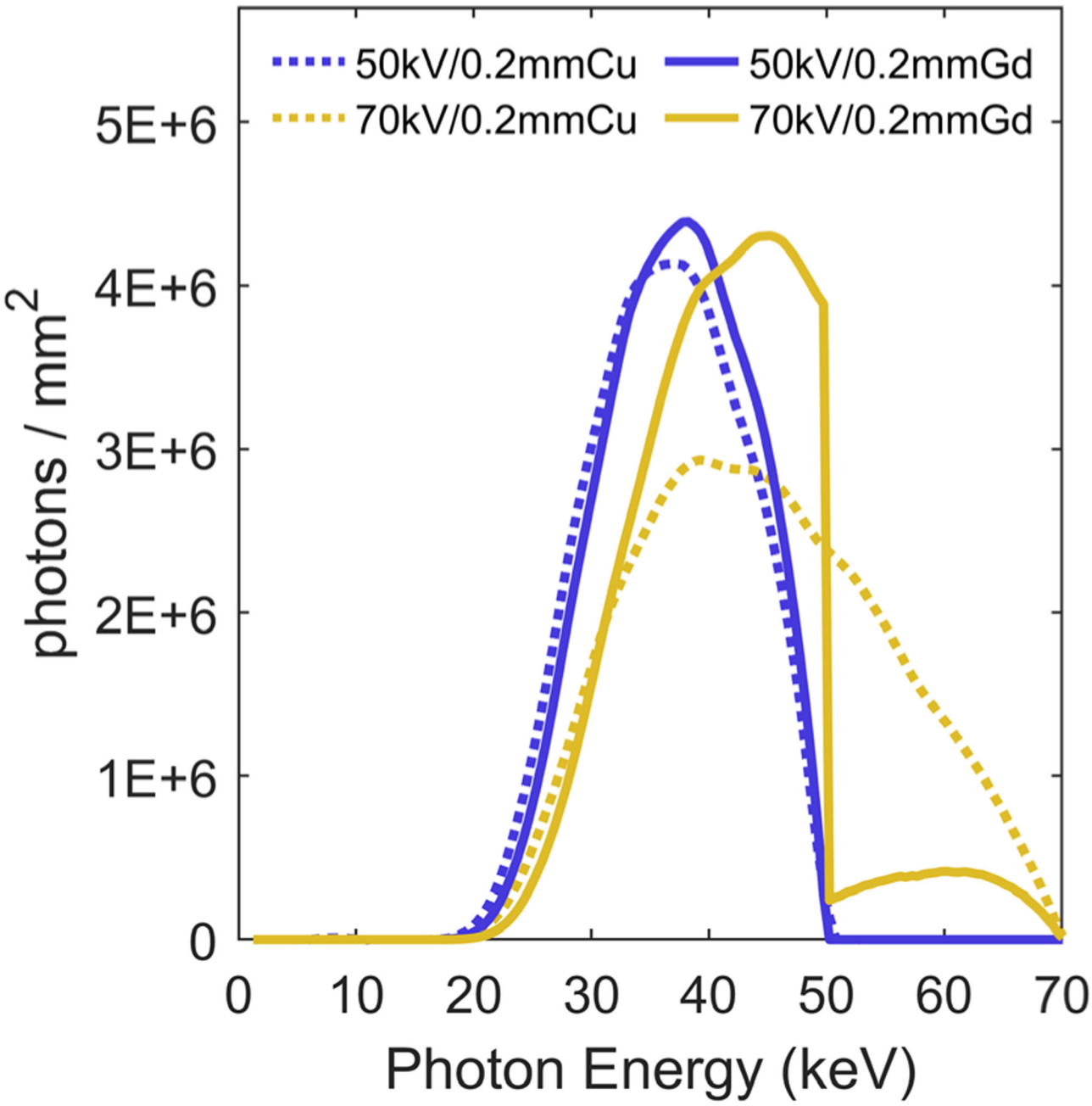

Fig. 3.

Modeled x-ray spectra generated for the 50 and 70 kV spectra with 0.2 mm Cu and 0.2 mm Gd filtration. The photon fluence is scaled to the air kerma (see Table I) that delivers a 6 mGy mean glandular dose for the V3 (median)-sized breast phantom.

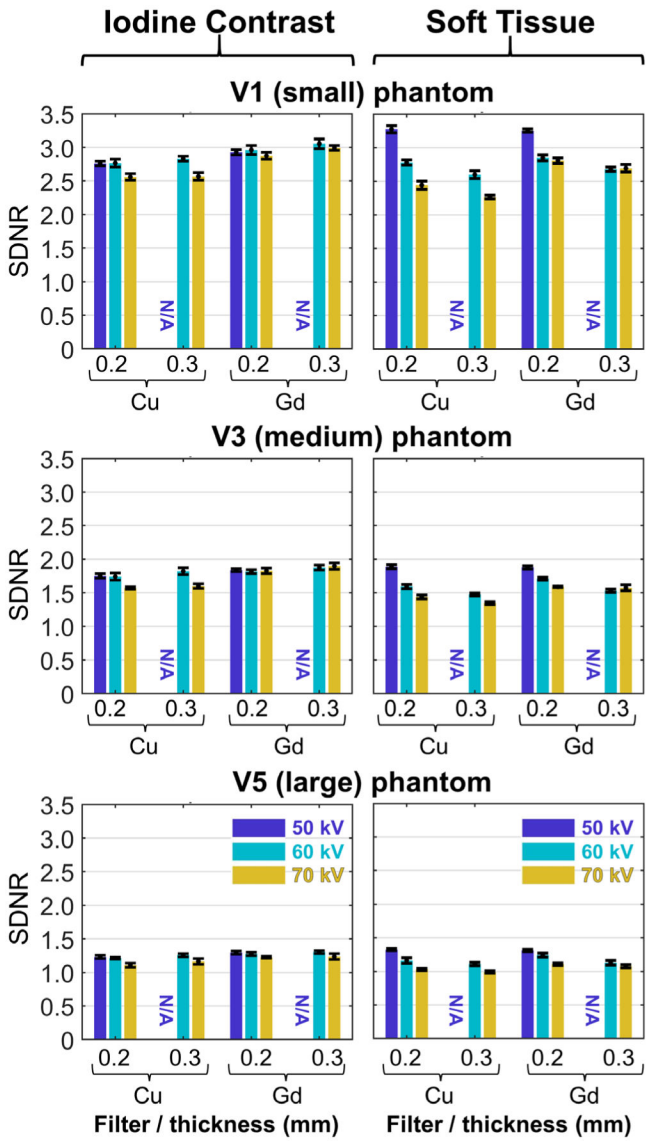

Fig. 4.

Signal-difference-to-noise ratio (SDNR) results measured for iodine contrast (left column) and soft tissue (right column) for phantom sizes V1, V3, and V5 using a constant mean glandular dose of 6 mGy. Several kV/filter combinations were beyond the tube power limitations of the scanner under investigation and are indicated by “N/A.” The SDNR value is the average and standard deviation (error bars) across seven consecutive slices centered about the central plane in the breast computed tomography scanner.

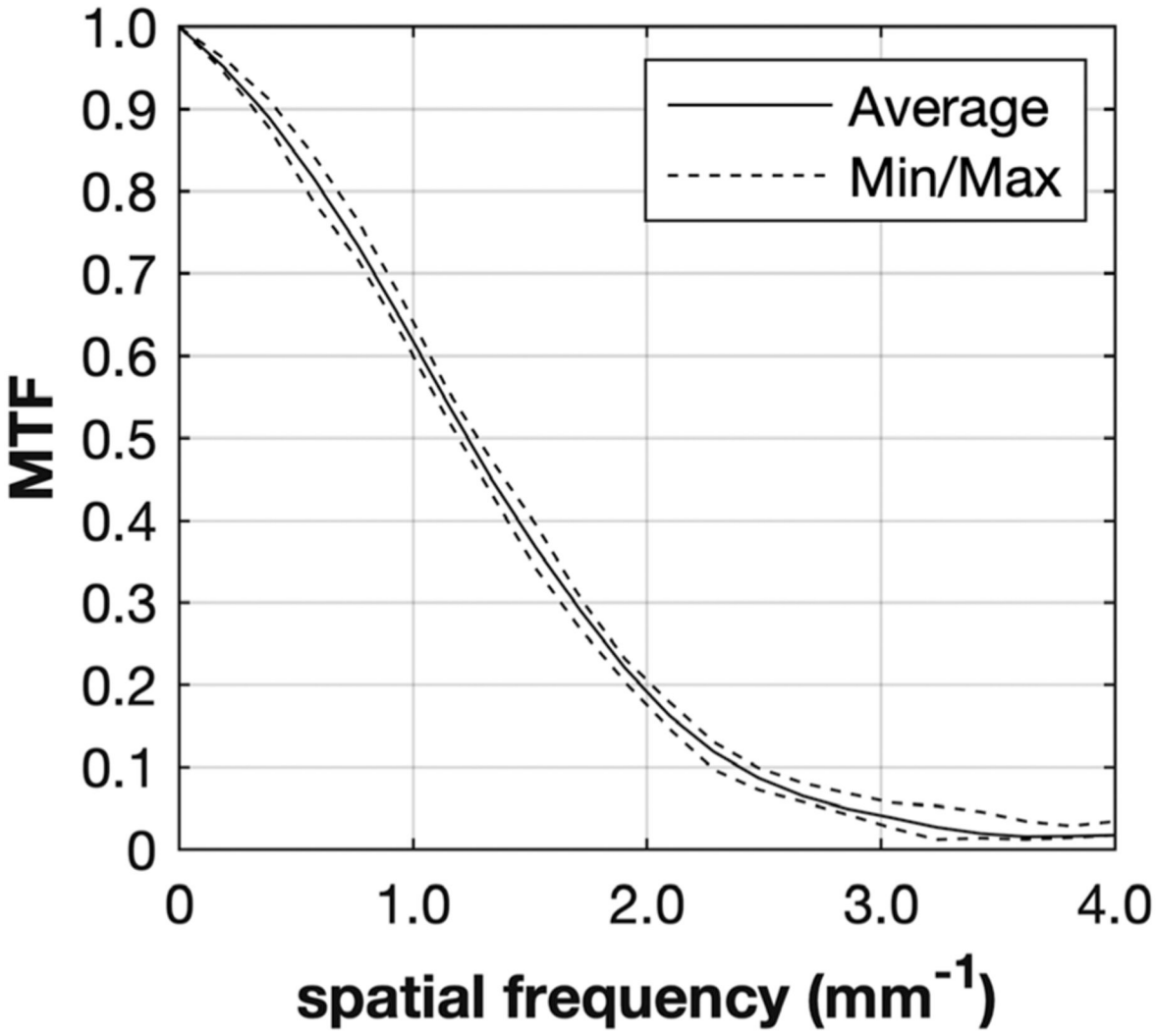

Fig. 5.

Radially averaged modulation transfer function for the median-sized (V3) phantom. The average value across all 10 kV/filter combinations and both imaging tasks is shown along with +/− one standard deviation from the mean.

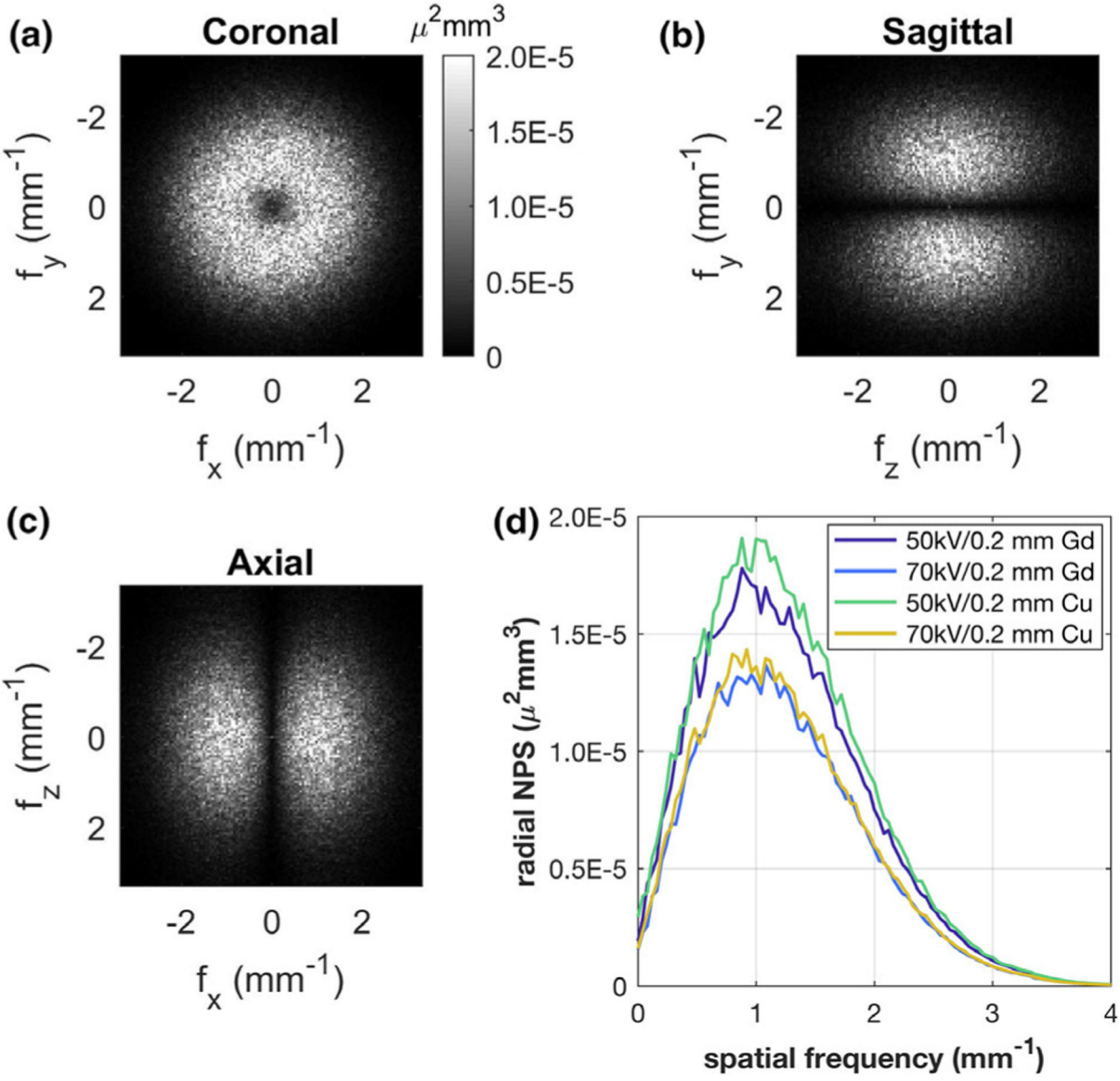

Fig. 6.

(a–c) Orthogonal central slices through the three-dimensional (3D) NPS measured in the reconstructed images of the V3 phantom scanned with 50 kV and 0.2 mm Gd filtration. Radially averaged central slices through the 3D NPS ($f_z = 0$) are also shown for a subset of 4 kV/filter combinations and the V3 phantom size.

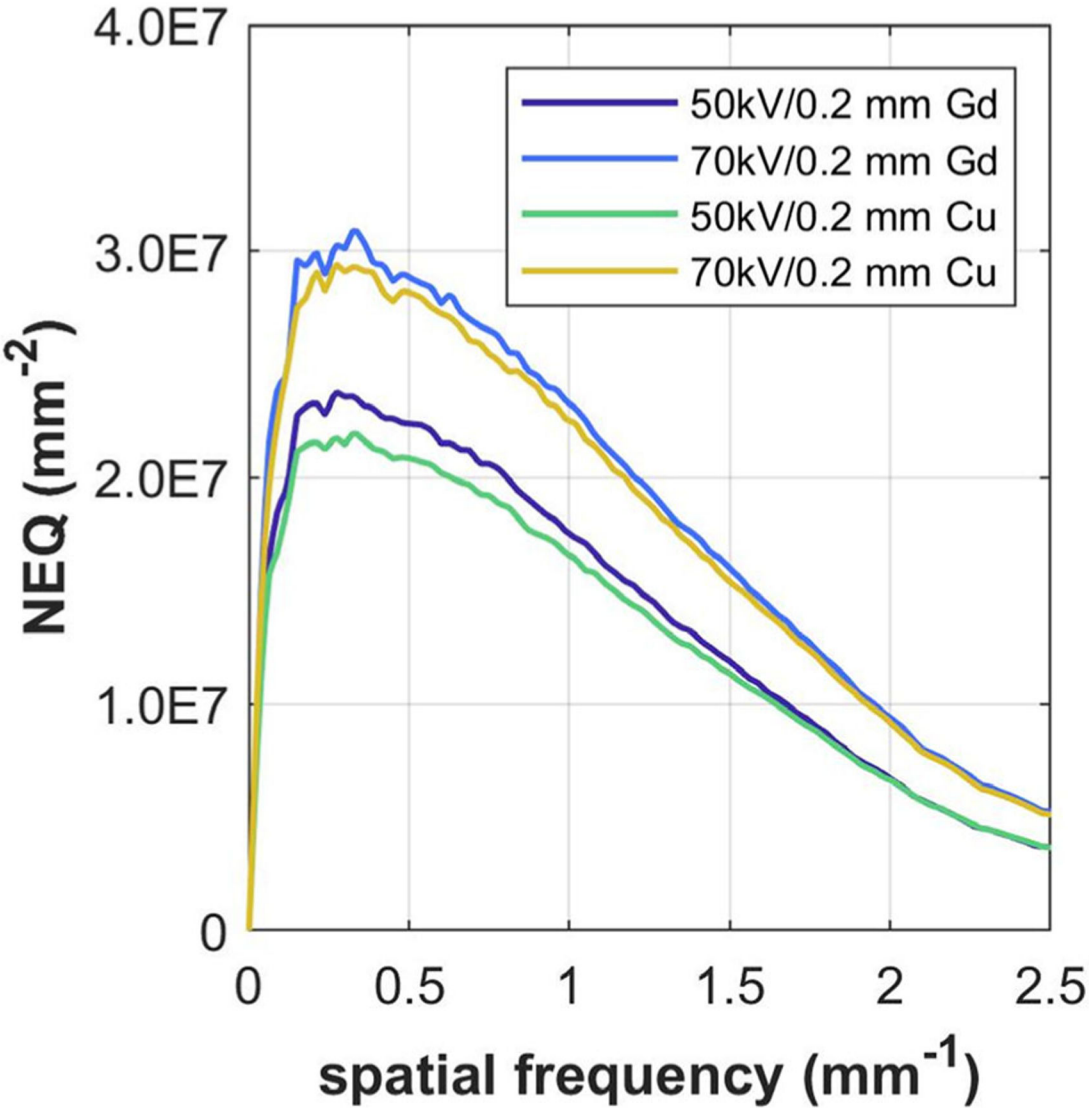

Fig. 7.

Comparisons of the two-dimensional noise equivalent quanta (NEQ) for the median-sized (V3) phantom at 6 mGy mean glandular dose for a subset of 4 kV/filter combinations. The results for 60 kV, 0.3 mm Gd, and 0.3 mm Cu filtration are not shown for ease in visual comparisons.

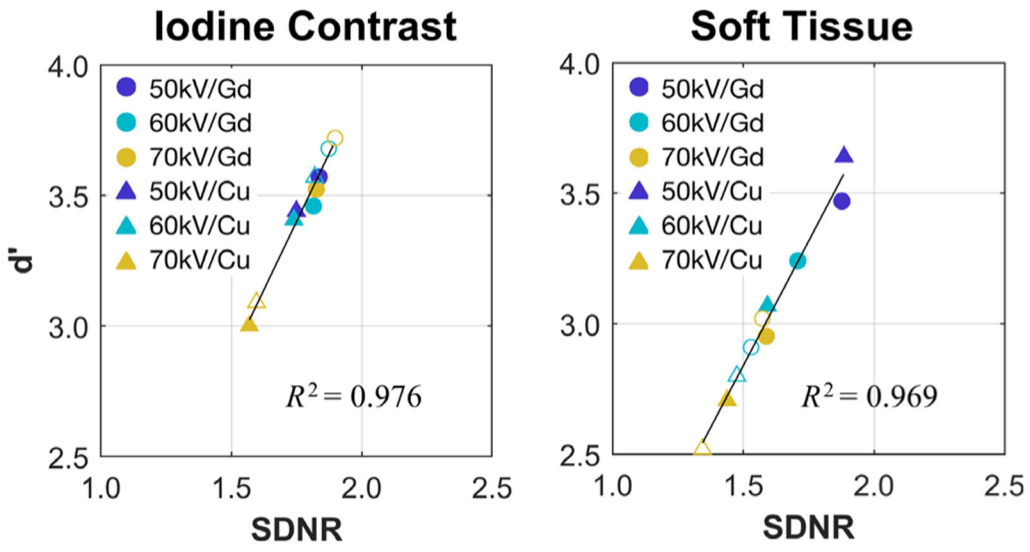

Fig. 8.

Correlation comparisons between the two-dimensional slice detectability index (d') measured in the frequency domain and the signal-difference-to-noise ratio measured in the image domain. Results are shown for the V3 phantom and all 10 kV/filter combinations for the iodine contrast and soft tissue tasks. Results for the thin filters (0.2 mm Gd/Cu) are shown using solid markers and thick filter results (0.3 mm Gd/Cu) are shown using outlined markers.

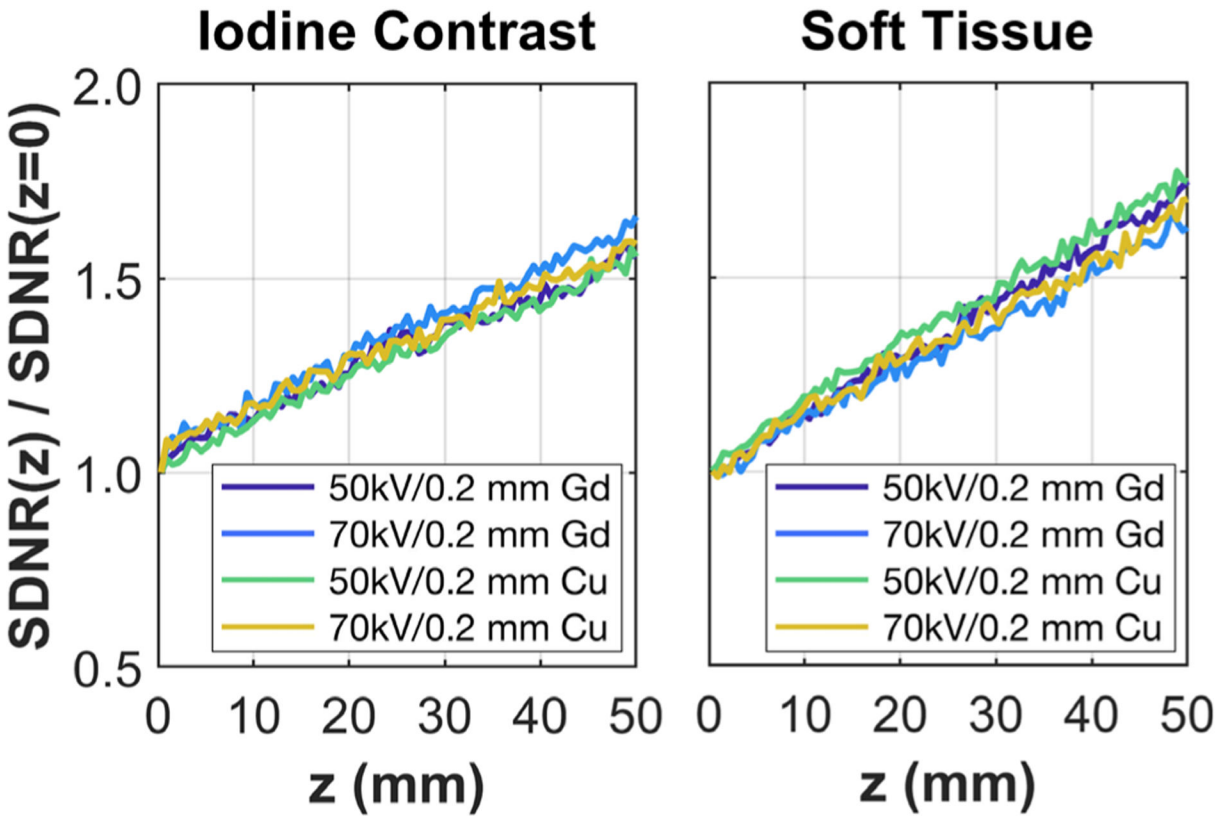

Fig. 9.

Signal-difference-to-noise ratio (SDNR) results for the V3 (median)-sized phantom from the posterior (z = 0 cm) to anterior (z = 50 mm) region of the contrast wells in the breast-shaped phantom. Results are shown for iodine contrast and soft tissue contrast tasks for tube potentials of 50 and 70 kV with either 0.2 mm Cu or 0.2 mm Gd added filtration. The y-axis is the SDNR as a function of z normalized to the SDNR at z = 0 (i.e., posterior boundary of scanner field of view).

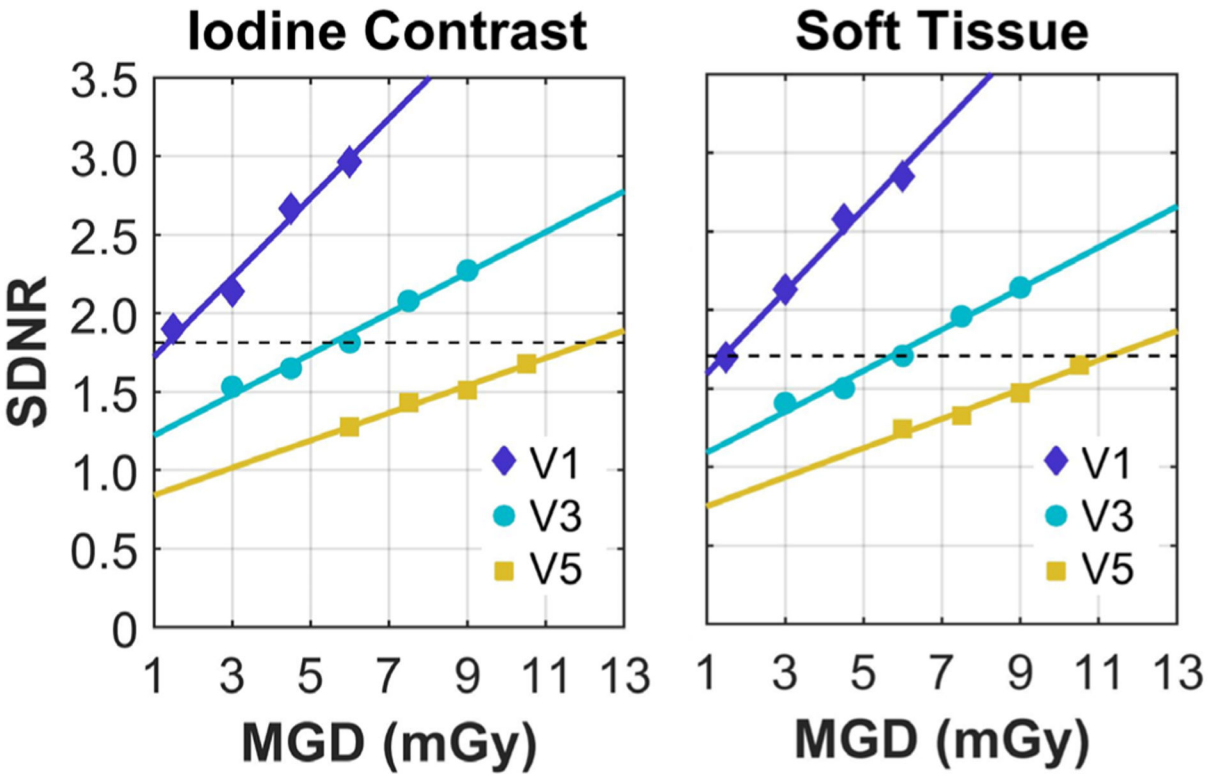

Fig. 10.

Signal-difference-to-noise ratio (SDNR) results at various mean glandular dose (MGD) levels for 60 kV with 0.2 mm Gd filtration. Results are shown for the V1, V3, and V5 phantoms along with a linear fit. The dashed line indicates the SDNR for the V3 phantom at 6 mGy and can be used to interpolate the dose that is necessary to provide identical image quality across all phantom sizes.

Table I.

Air kerma values required to deliver a mean glandular dose (MGD) of 6 mGy for the V1 (small), V3 (medium), and V5 (large) phantom sizes and tube potentials of 50, 60, and 70 kV. The MGD was calculated using published DgN coefficients for the realistic breast-shaped phantoms,[11] and half value layer measurements (shown in italic) from the Doheny breast computed tomography scanner.

		Air Kerma (mGy)		
Filtration	**Phantom Size**	**50 kV**	**60 kV**	**70 kV**
0.2 mm Cu	V1	8.53	7.99	7.73
	V3	8.65	7.97	7.64
	V5	9.06	8.23	7.83
	HVL (mm Al)	*2.86*	*3.52*	*4.01*
0.3 mm Cu	V1	8.01	7.53	7.30
	V3	8.01	7.40	7.12
	V5	8.31	7.57	7.22
	HVL (mm Al)	*3.44*	*4.31*	*4.96*
0.2 mm Gd	V1	8.27	7.90	7.70
	V3	8.33	7.87	7.62
	V5	8.69	8.13	7.82
	HVL (mm Al)	*3.11*	*3.61*	*3.97*
0.3 mm Gd	V1	7.81	7.46	7.37
	V3	7.76	7.33	7.22
	V5	8.02	7.49	7.35
	HVL (mm Al)	*3.73*	4.41	4.64